

# Simulation of Borehole Resistivity Tools Through Metal Casing at Different Frequencies Using a Goal Oriented $hp$ Finite Element Method (FEM).

D. Pardo, C.Torres-Verdín, L. Demkowicz

**Abstract**—We simulate a through-casing resistivity tool (TCRT) operating at different frequencies in a borehole environment for the assessment of rock formation properties. Rock formations are assumed to exhibit axial symmetry around the axis of a vertical borehole. The simulations are performed with a goal-oriented  $hp$ -adaptive FEM that delivers exponential convergence rates in terms of the *quantity of interest* (for example, the second vertical difference of the electric potential) against the CPU time.

Numerical results illustrate the efficiency and accuracy of the method, allowing for high-accuracy simulations of logging instruments in the presence of highly conductive casing. The study of different tool configurations show the advantages of using calibrated instruments with toroid antennas located on the borehole walls. We quantify the agreement between numerical and analytical results when the latter are available.

## I. INTRODUCTION

Casing is commonly used to avoid collapse of wells in oil fields by inserting metallic pipes into the borehole. This casing highly attenuates electromagnetic fields, and therefore, the assessment of rock formation properties behind casing becomes challenging. Nevertheless, it was shown in [1] that the second vertical difference of the electric potential measured on the receiving electrodes (or antennas) is proportional to the leakage of current into the formation, and therefore, it is feasible to determine the conductivity of rock formations behind casing via either analytical or numerical methods.

While most analytical methods cannot be applied to complex geometries, simulation of TCRT via numerical methods is rather challenging due to the presence of casing. Here, we develop a novel numerical method based on a self-adaptive, goal oriented  $hp$ -FEM that accurately simulates these logging instruments. This approach is needed to design and predict the behavior of TCRT, as well as for solving the related *inverse* problem.

Previous research in this area includes the work of Kaufmann [1] and Vail *et. al.* [2] dealing with analytical approximations and the design of calibrated instruments, respectively. It is also remarkable the contributions of Schenkel and Morrison [3] studying the possibility of cross-well resistivity surveys if one well is cased, and Wu and Habashy [4], who illustrated the response of a TCRT as a function of the frequency. In this paper, we compare Kaufmann's approximation formulas against the exact solution as well as numerical simulations. Moreover,

we provide numerical results simulating the response of calibrated instruments in the presence of damaged casing, we study optimal placement of antennas within the borehole, and we describe numerical results at different frequencies.

First, we describe the specifics of the assumed logging instrument and borehole environment. Next, we derive an analytical solution for a simplified borehole and rock formation model. We briefly introduce the numerical methodology used for solving our problems, and we verify the numerical results by comparing them against the analytical solution for the simplified model. In Section V, we present numerical results corresponding to the original problem of interest. Finally, we discuss the findings of our research, with conclusions presented thereafter. We also include an appendix containing the main theoretical ideas behind the self-adaptive goal-oriented  $hp$ -FEM.

All problems and applications considered in this article are assumed to be axisymmetric, that is, the geometry, material properties, and distribution of antennas is axial symmetric with respect a line (the axis of symmetry).

## II. TCRT APPLICATION

In this section, we introduce our TCRT application of interest. Using cylindrical coordinates  $(\rho, \phi, z)$ , we consider the following geometry, sources, receivers, and materials (illustrated in Fig. 1):

- One 10 cm-long (infinitely thin) source electrode located on the axis of symmetry and moving along the  $z$ -axis.
- Three 5 cm-long (infinitely thin) receiving electrodes located 150 cm, 175 cm, and 200 cm above the source electrode, on the axis of symmetry.
- Borehole: a cylinder  $\Omega_I$  of radius 10 cm surrounding the axis of symmetry ( $\Omega_I = \{(\rho, \phi, z) : \rho \leq 10 \text{ cm}\}$ ), with resistivity  $R=0.1 \Omega \cdot \text{m}$ .
- Casing: a steel casing  $\Omega_{II}$  of width 1.27 cm surrounding the borehole ( $\Omega_{II} = \{(\rho, \phi, z) : 10 \text{ cm} \leq \rho \leq 11.27 \text{ cm}\}$ ), with resistivity  $R=0.000001 \Omega \cdot \text{m} = 10^{-6} \Omega \cdot \text{m}$ .
- Formation Material I: a subdomain  $\Omega_{III}$  defined by  $\Omega_{III} = \{(\rho, \phi, z) : \rho > 11.27 \text{ cm}, 0 \text{ cm} \leq z \leq 100 \text{ cm}\}$ , with resistivity  $R=1 \Omega \cdot \text{m}$ .
- Formation Material II: a subdomain  $\Omega_{IV}$  defined by  $\Omega_{IV} = \{(\rho, \phi, z) : \rho > 11.27 \text{ cm}, -50 \text{ cm} \leq z < 0 \text{ cm}\}$ , with resistivity  $R=10000 \Omega \cdot \text{m}$ .

- Formation Material III: a subdomain  $\Omega_V$  defined by  $\Omega_V = \{(\rho, \phi, z) : \rho > 11.27 \text{ cm}, z < -50 \text{ cm} \text{ or } z > 100 \text{ cm}\}$ , with resistivity  $R=100 \Omega \cdot \text{m}$ .

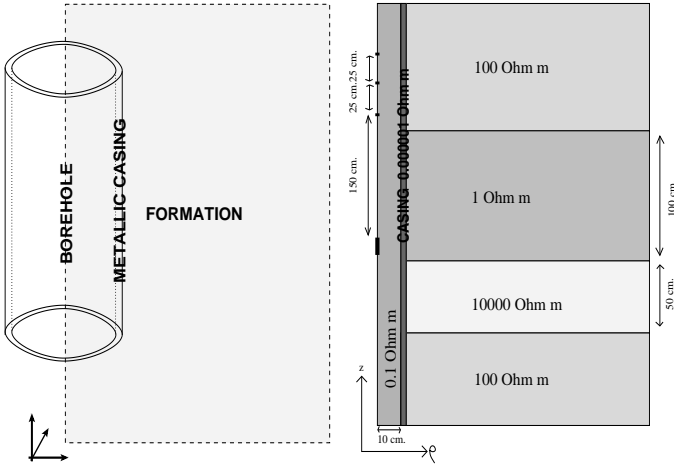


Fig. 1. Geometry of a Through Casing Resistivity Tool (TCRT) problem. The model consists of one transmitter and three receiver electrodes, a conductive borehole, a metallic casing, and four layers in the formation material with varying resistivities. Left panel: 3D view. Right panel: 2D cross section using cylindrical coordinates.

#### A. Objective.

The objective of the simulation is to determine the second difference of the potential  $\Delta^2 V$  between the three receiving electrodes, namely,

$$\Delta^2 V = (u(r_1) - u(r_2)) - (u(r_2) - u(r_3)), \quad (1)$$

where  $r_1$ ,  $r_2$ , and  $r_3$  are the locations of the three receiving electrodes. Notice that the functional  $\Delta^2 : V \rightarrow \mathbb{R}$  defined by  $\Delta^2(u) = u(r_1) - 2u(r_2) + u(r_3)$  is not continuous (in the corresponding Finite Element space) and it should be replaced by a post-processing formula (see [5], [6]).

#### B. Computational domain.

The problem is formulated in the whole space. Construction of infinite elements (see [7] for details), or other techniques are unnecessary because the solution decays as  $\frac{1}{\sigma r}$  for  $r \rightarrow \infty$ , where  $\sigma$  is the conductivity of the medium and  $r$  is the distance between the source and the target point. We may simply truncate the domain at a large distance, and apply a PEC (or Neumann) boundary condition along the truncated boundary.

For the logging applications described in this article, we apply a PEC boundary condition at distances (from the transmitter electrode/antenna) ranging from 2 to 20 kilometers in the vertical direction (depending upon the frequency and resistivity of casing) and 1 kilometer in the horizontal direction.

### III. ANALYTICAL SOLUTION

For testing purposes, we derive an analytical solution for a simplified model problem, composed of a borehole, a metallic casing, and a single material in the formation. That is, we consider a source point electrode located at  $(\rho = 0, z = 0)$

radiating into a region with three different conductivities:  $\sigma_1$  (for  $r \leq \rho_1$ ),  $\sigma_2$  (for  $\rho_1 < \rho \leq \rho_2$ ), and  $\sigma_3$  (for  $\rho_2 < \rho$ ), respectively.

We wish to solve the partial differential equation (in cylindrical coordinates),

$$-\frac{1}{\rho} \frac{\partial}{\partial \rho} \left( \sigma \rho \frac{\partial u}{\partial \rho} \right) - \sigma \frac{\partial^2 u}{\partial z^2} = \delta(\rho) \delta(z), \quad (2)$$

where  $\delta$  is the Dirac's delta function, with the decay condition,

$$u(\rho, z) \rightarrow 0, \quad \text{as } \rho, z \rightarrow \infty, \quad (3)$$

and an additional condition resulting from the axisymmetry assumption, i.e.,

$$\frac{\partial u}{\partial \rho}(0, z) = 0. \quad (4)$$

By taking the Fourier transform in  $z$ , we obtain,

$$-\sigma \left( \frac{1}{\rho} \frac{\partial}{\partial \rho} \rho \frac{\partial \tilde{u}}{\partial \rho} \right) + \sigma k_z^2 \tilde{u} = \delta(\rho), \quad (5)$$

where  $\tilde{u}$  is the Fourier transform of  $u$ , and  $k_z$  is the Fourier variable. The solution of (5) consists of three branches,

$$\tilde{u}(\rho) = \begin{cases} \tilde{u}_1(\rho) & 0 < \rho < \rho_1 \\ \tilde{u}_2(\rho) & \rho_1 < \rho < \rho_2 \\ \tilde{u}_3(\rho) & \rho_2 < \rho \end{cases}, \quad (6)$$

that are solutions of the homogeneous ordinary differential equation,

$$-\frac{1}{\rho} (\tilde{u}' + \rho \tilde{u}'') + k_z^2 \tilde{u} = 0, \quad (7)$$

with a source term condition, the decay condition (3), and four additional interface conditions, namely:

$$\tilde{u}_1(\rho_1) = \tilde{u}_2(\rho_1), \quad (8)$$

$$\tilde{u}_2(\rho_2) = \tilde{u}_3(\rho_2), \quad (9)$$

$$\sigma_1 \tilde{u}_1'(\rho_1) = \sigma_2 \tilde{u}_2'(\rho_1), \quad \text{and}, \quad (10)$$

$$\sigma_2 \tilde{u}_2'(\rho_2) = \sigma_3 \tilde{u}_3'(\rho_2). \quad (11)$$

By multiplying (7) by  $\rho^2$ , and with the change of variables  $x = \rho \cdot k_z$ , we obtain the modified Bessel equation,

$$x^2 \tilde{u}'' + x \tilde{u}' - x^2 \tilde{u} = 0. \quad (12)$$

The corresponding space of solutions is given by the span of any two linearly independent solutions of (12). For example,

$$\tilde{u}(x) = C_1 I_0(x) + C_2 K_0(x), \quad (13)$$

where  $C_1$  and  $C_2$  are constants to be determined, and  $I_0$  and  $K_0$  are the so called *Bessel functions of imaginary argument*, also referred to as the *modified Bessel functions*. Consequently,

$$\tilde{u}_1(\rho, k_z) = C_1 I_0(k_z \rho) + C_2 K_0(k_z \rho), \quad (14)$$

$$\tilde{u}_2(\rho, k_z) = C_3 I_0(k_z \rho) + C_4 K_0(k_z \rho), \quad \text{and}, \quad (15)$$

$$\tilde{u}_3(\rho, k_z) = C_5 I_0(k_z \rho) + C_6 K_0(k_z \rho). \quad (16)$$

If  $k_z > 0$  (thus  $k_z \rho > 0$ ) the source term condition implies  $C_2 = \frac{1}{(2\pi)^{3/2} \sigma_1}$  (see [6] for details), and condition (3) implies  $C_5 = 0$ . However, if  $k_z < 0$ , these conditions

imply a non-trivial combination of complex valued constants  $C_i, i = 1 \dots 6$ . Thus, the choice of the two linearly independent solutions made in (13) is inadequate to represent the solution when  $k_z < 0$  (in the sense that algebraic derivations as well as computations become both rather challenging and tedious). Furthermore,  $K_0$  is not symmetric ( $K_0(x) \neq K_0(-x)$ ), and by using the representation (14)-(15) we lose the symmetry properties of  $\tilde{u}(k_z)$ . Therefore, we select the following new representation for our solution:

$$\tilde{u}(\rho, k_z) = C_1 I_0(|k_z|\rho) + C_2 K_0(|k_z|\rho). \quad (17)$$

Accordingly, in terms of  $\tilde{u}_1, \tilde{u}_2$ , and  $\tilde{u}_3$ , we have:

$$\tilde{u}_1(\rho, k_z) = C_1 I_0(|k_z|\rho) + C_2 K_0(|k_z|\rho), \quad (18)$$

$$\tilde{u}_2(\rho, k_z) = C_3 I_0(|k_z|\rho) + C_4 K_0(|k_z|\rho), \quad \text{and}, \quad (19)$$

$$\tilde{u}_3(\rho, k_z) = C_5 I_0(|k_z|\rho) + C_6 K_0(|k_z|\rho). \quad (20)$$

Now, for every  $k_z$  the source term condition implies  $C_2 = \frac{1}{(2\pi)^{3/2}\sigma_1}$ , and condition (3) implies  $C_5 = 0$ .

Equations (8) and (10) imply,

$$C_1 I_0(x_1) + C_2 K_0(x_1) = C_3 I_0(x_1) + C_4 K_0(x_1), \quad \text{and}, \quad (21)$$

$$C_1 I_1(x_1) - C_2 K_1(x_1) = \mu_{21}[C_3 I_0(x_1) + C_4 K_0(x_1)], \quad (22)$$

where  $\mu_{21} = \sigma_2/\sigma_1$ , and  $x_1 = |k_z|\rho_1$ . By solving for  $C_3$  and  $C_4$ , we obtain,

$$C_3 = [1 - AK_0(x_1)I_1(x_1)]C_1 + [AK_0(x_1)K_1(x_1)]C_2 \quad \text{and}, \quad (23)$$

$$C_4 = [AI_0(x_1)I_1(x_1)]C_1 + [1 - AI_0(x_1)K_1(x_1)]C_2, \quad (24)$$

where  $A = (1 - 1/\mu_{21})x_1$ . Similarly, using equations (9) and (11), and solving for  $C_3$  and  $C_4$ , we obtain,

$$C_3 = [BK_0(x_2)K_1(x_2)]C_6, \quad \text{and}, \quad (25)$$

$$C_4 = [1 - BI_0(x_2)K_1(x_2)]C_6, \quad (26)$$

where  $x_2 = |k_z|\rho_2$ ,  $B = (1 - \mu_{32})x_2$ , and  $\mu_{32} = \sigma_3/\sigma_2$ . The system of equations (23), (24), (25), and (26) leads to the following solution for  $C_1$ :

$$C_1 = \frac{\begin{vmatrix} -AK_0(x_1)K_1(x_1)C_2 & -BK_0(x_2)K_1(x_2) \\ (1 - AI_0(x_1)K_1(x_1))C_2 & 1 - BI_0(x_2)K_1(x_2) \end{vmatrix}}{\begin{vmatrix} 1 - AK_0(x_1)I_1(x_1) & -BK_0(x_2)K_1(x_2) \\ -AI_0(x_1)I_1(x_1) & 1 - BI_0(x_2)K_1(x_2) \end{vmatrix}}. \quad (27)$$

By making use of (18), the identity  $C_2 = \frac{1}{(2\pi)^{3/2}\sigma_1}$  and (27), we obtain the explicit solution for the potential along the borehole in the Fourier domain. Application of the inverse Fourier transform yields the final solution, namely,

$$u(\rho, z) = \frac{1}{\sqrt{2\pi}} \begin{cases} \int_{-\infty}^{\infty} \tilde{u}_1(\rho, k_z) \exp^{jk_z \cdot z} dk_z & 0 < \rho < \rho_1 \\ \int_{-\infty}^{\infty} \tilde{u}_2(\rho, k_z) \exp^{jk_z \cdot z} dk_z & \rho_1 < \rho < \rho_2 \\ \int_{-\infty}^{\infty} \tilde{u}_3(\rho, k_z) \exp^{jk_z \cdot z} dk_z & \rho_2 < \rho \end{cases} \quad (28)$$

#### IV. NUMERICAL METHOD: A GOAL-ORIENTED $hp$ -FEM

We are interested in solving numerically the variational problem,

$$\begin{cases} \text{Find } u \in u_D + V \\ b(u, v) = f(v) \quad \forall v \in V, \end{cases} \quad (29)$$

where the bilinear form  $b$  corresponds to either the conductive media equation (direct current case) or the reduced wave equation (alternate current case) in the frequency domain. Here

- $u_D$  is an arbitrary function satisfying essential (Dirichlet) BC.
- $V$  is a (Hilbert) space with an inner product  $(\cdot, \cdot)$ .
- $f \in V'$  is a linear and continuous functional on  $V$ .
- $b$  is a bilinear and symmetric form.

Our objective is to determine the *quantity of interest*  $L(u) = \Delta^2 V(u)$ , where  $\Delta^2 V$  is defined by (1), and  $u$  is the solution of the problem (29). In order to attain this objective, our numerical method should overcome the following difficulties:

- It should simulate large computational domains efficiently, since the effect of metallic casing requires a large computational domain in the vertical direction (several miles).
- It should deal with the strong variation in conductivity that occurs between the casing and the rock formation (up to ten orders of magnitude).
- It should accommodate elongated elements with large aspect ratio (up to  $10^3 - 10^5$ ), which are required by the geometry of the casing.
- It should accurately compute  $L(u)$ , which is expected to be several orders of magnitude smaller than the solution itself. The total dynamic range (quotient between largest value of the solution and  $L(u)$ ) is expected to be about  $10^{13}$ .

The numerical method we present next is based on a self-adaptive goal-oriented  $hp$  FEM, and it overcomes all difficulties mentioned above.

##### A. $hp$ -Finite Elements (FE)

Our numerical technique is based on  $hp$ -FE discretizations of electromagnetic problems. Here  $h$  stands for the element size, and  $p$  denotes the polynomial element order (degree) of approximation, both varying *locally* throughout the grid.

The main advantage of the  $hp$ -FEM is given by the following result:

*For an optimal sequence of grids, both in terms of element size  $h$  and polynomial order of approximation  $p$ , the corresponding sequence of solutions converges exponentially to the exact solution with respect to the number of unknowns (as well as the CPU time), independently of the number, intensity, and/or distribution of singularities in the solution.*

A proof of this result is long and tedious, and it can be found in [8], [9], [10].

### B. A self-adaptive goal-oriented algorithm

The algorithm presented in [6] produces a sequence of optimally  $hp$ -refined meshes that delivers exponential convergence rates in terms of a prescribed quantity of interest against the size of the discrete problem or CPU time. A given (coarse)  $hp$  mesh is first refined globally in *both*  $h$  and  $p$  to yield a *fine mesh*, *i.e.* each element is broken into four new elements (eight in 3D), and the discretization order of approximation  $p$  is raised uniformly by one. Then, the problem of interest on the fine mesh is solved. The next *optimal coarse mesh* is then determined as the one that maximizes the decrease of the *projection based interpolation error* averaged by the added number of unknowns. Since the mesh optimization process is based on minimizing the interpolation error rather than the residual, the algorithm is problem independent, and it can be applied to nonlinear and eigenvalue problems as well. A more detailed description of this algorithm is presented in the Appendix.

### C. Verification of the numerical method

Fig. 2 compares four solutions corresponding to the simplified TCRT problem presented in Section III. These solutions are:

- 1) Kaufmann approximation formulas [1],
- 2) the analytical solution for the second derivative of the potential with respect to the vertical direction,
- 3) the analytical solution for the normalized second difference of the potential (using three electrodes separated by 25 cm. each), and,
- 4) the numerical solution for the normalized second difference of the potential, which have been obtained using the goal-oriented  $hp$ -adaptive FEM presented in this section.

Results indicate the agreement of all solutions, with the exception of Kaufmann approximation formulas, which deliver larger errors (up to 25% relative errors in the linear scale) as the resistivity of the rock formation increases.

## V. NUMERICAL RESULTS

In this section, we present the final log corresponding to our TCRT problem at DC. Then, we consider the more realistic case of imperfect casing. Finally, we consider a nonzero frequency and we study the dependence of the solution with respect to frequency.

### A. TCRT at DC.

At this point, we present the main result of our computations at DC for the TCRT problem, *i.e.*, the second difference of the potential on the receiving electrodes as we move the logging instrument in the  $z$  direction. This result is displayed in Fig. 3 (left), where the horizontal axis corresponds to the second difference of the potential in micro Volts, and plotted with a logarithmic scale. The vertical axis indicates the vertical position of the second receiving electrode. If we consider a casing of resistivity  $10^{-7} \Omega \cdot m$  (as opposed to  $10^{-6} \Omega \cdot m$ ), similar results are obtained, with the exception that the scales are shifted by approximately a factor of 50 (see right panel

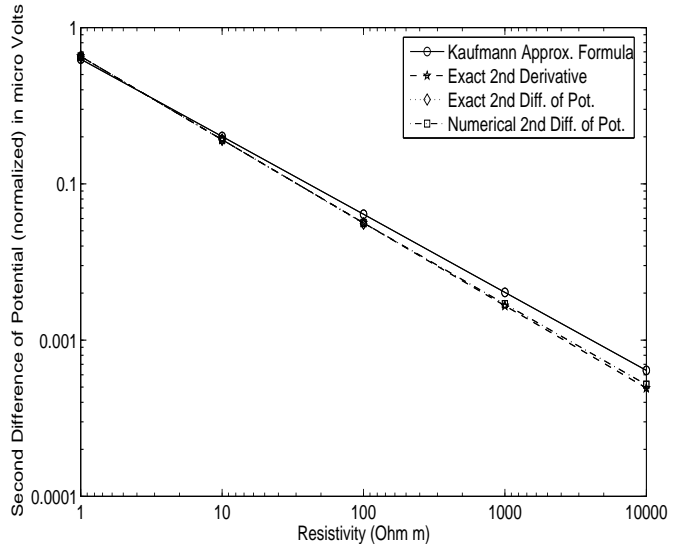


Fig. 2. Through Casing Resistivity Tool (TCRT) problem with a single material on the formation and the electrodes arrangement described in Fig. 1. Resistivity of the rock formation against the second difference of potential (normalized) in micro Volts using four different solution methods: (a) Kaufmann approximation formulas, (b) the analytical solution for the second derivative of the potential, (c) the analytical solution for the second difference of the potential, and (d) a numerical approximation of the second difference of the potential.

of Fig. 3). These results also indicate that when a layer in the formation is not thick enough, the corresponding simulated tool measurements *do not agree* with the *ad hoc* solution obtained by patching up analytical one-layer solutions.

In Fig. 4 we display the error and number of unknowns of the associated system of linear equations vs. the position in the  $z$ -axis of the second receiving electrode. With fewer than 9000 unknowns, we guarantee a relative error in the second difference of the potential below 0.25 %. Thus, our numerical method is both efficient and accurate. Notice that the number of unknowns increases with respect to the position of the receiving electrode. This is because as we move the logging instrument (from bottom to top) we employ the grid from the previous position as the new starting point.

### B. The Case of Damaged Casing.

In this section, we describe a method that accounts for possible imperfections on a metallic casing. Typically, due to corrosion and damage, a casing is not uniform in thickness along the borehole, and hence it contains zones with different conductivities. Furthermore, the distribution of these imperfections on the casing is frequently unknown *a priori*. However, the solution is extremely sensitive to the thickness and conductivity of the casing.

We consider a damaged casing and a logging tool containing five electrodes as displayed in Fig. 5. Enumerating them in ascending order from bottom to top, we consider the following two situations:

- 1) CASE A. We excite electrodes 1 and 5 with a source term corresponding to 1 A and -1 A, respectively. We define  $u_1$  and  $u_2$  as the first difference of the potential between electrodes 3 and 4, and 2 and 3, respectively. Finally, we compute  $\alpha = \frac{u_1}{u_2}$ .

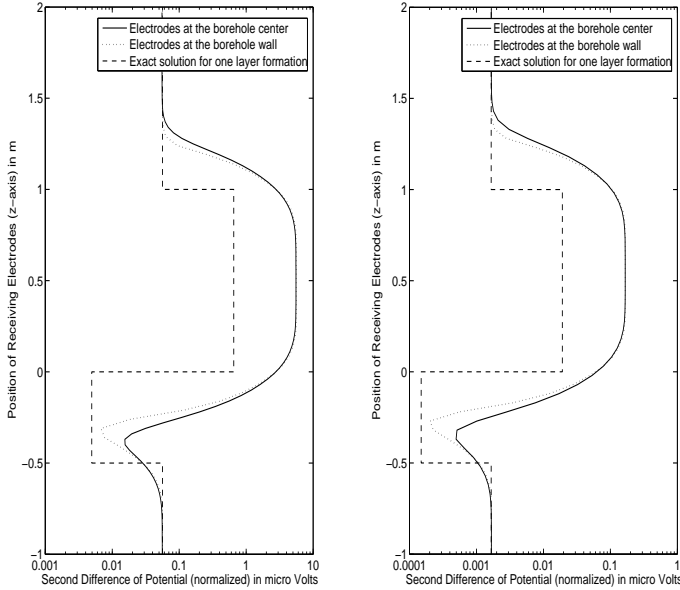


Fig. 3. TCRT problem. Second differences of the potential (micro Volts on logarithmic scale) vs. position in the  $z$ -axis of the second receiving electrode (in meters). Resistivity of the casing is equal to  $10^{-6} \Omega \cdot m$  (left panel) and  $10^{-7} \Omega \cdot m$  (right panel), respectively

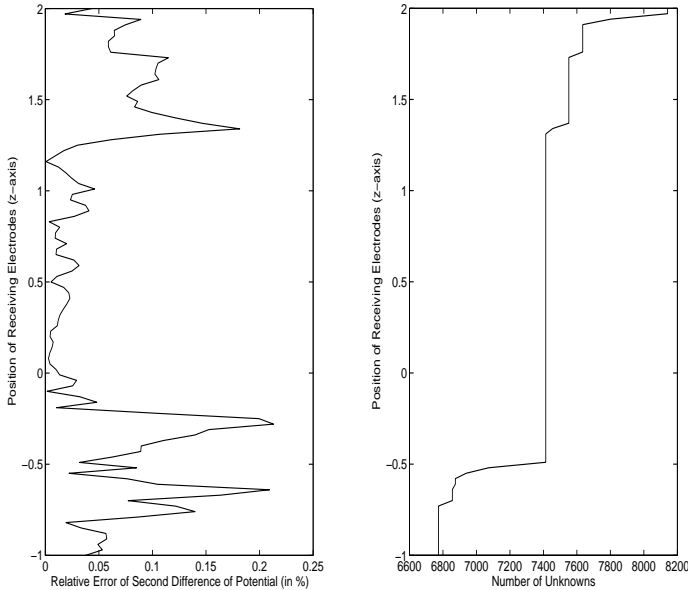


Fig. 4. TCRT problem. Relative error (left panel) of the second difference of potential (in percentage) and number of unknowns (right panel) of the corresponding linear system of equations against position in the  $z$ -axis of the receiving electrode (in meters).

2) CASE B. We excite electrode 1 with a source term corresponding to 1 A. We define  $u'_1$  and  $u'_2$  as the first difference of the potential between electrodes 3 and 4, and 2 and 3, respectively. Finally, we compute the quantity  $\beta = u'_1 - \alpha u'_2$ , where  $\alpha$  has been obtained from case A. In this expression,  $\beta$  is an approximation to the second difference of the potential that accounts for possible casing imperfections.

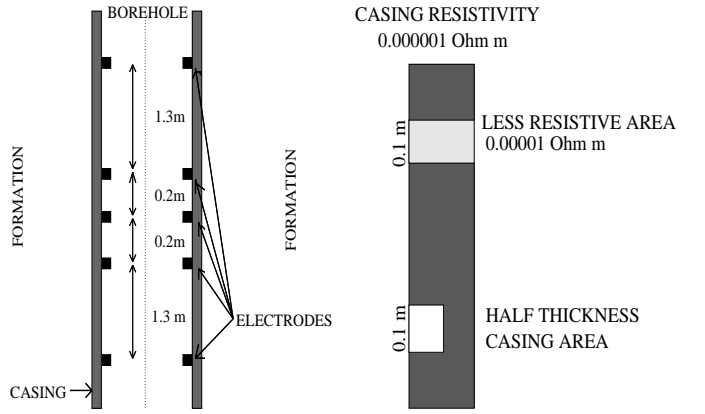


Fig. 5. Geometry of the TCRT problem for a damaged casing. Electrode arrangements (left panel) and casing structure (right panel).

The final log corresponding to the imperfect casing with the formation materials defined in Section V is shown in Fig. 6. The second difference of potential for a non-calibrated instrument is no longer proportional to the rock formation conductivity due to the effect of imperfect casing. Nevertheless, the use of a calibrated TCRT as the one described here permits us to obtain results that display an acceptable agreement with those corresponding to the case of perfect casing.

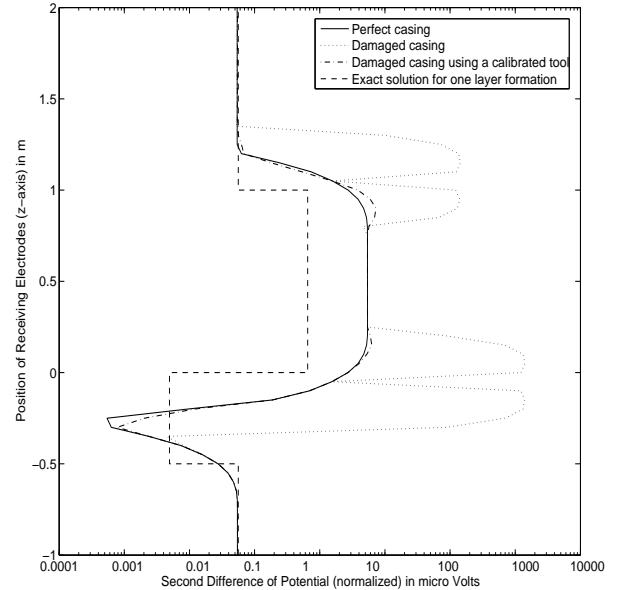


Fig. 6. TCRT problem. Second differences of the potential (micro Volts on logarithmic scale) vs. position in the  $z$ -axis of the second receiving electrode (in meters). We consider the cases of perfect casing, imperfect/damaged casing, and imperfect casing using a calibrated TCRT.

For more complex TCRT, see [2], [3] and references therein, where they describe different possibilities for arrangement of the electrodes/antennas and provide results for a number of simulations.

### C. TCRT at AC.

In this section, we consider the application described on Section II at different frequencies assuming a casing of resistivity  $10^{-5} \text{ Ohm} \cdot m$ , one transmitter antenna and two receiver

antennas located 1.65m and 1.85m above the transmitter antenna, respectively. We consider toroidal antennas with an imposed current equivalent to that of 1 Ampere in a Vertical Electrical Dipole (VED), also known as Hertzian dipole. Using cylindrical coordinates, the corresponding exact solution in a homogeneous space is given by (see [11], page 47):

$$\mathbf{H}(\rho) = \hat{\phi} I j k \frac{e^{-jkd}}{4\pi d} \left[ 1 - \frac{j}{kd} \right] \frac{\rho}{d}, \quad (30)$$

where  $k = \sqrt{\omega^2 \epsilon - j\omega \epsilon}$  is the wave number,  $I$  is the electric current, and  $d$  is the distance from the transmitter to the receiver antenna.

We consider two different types of toroidal antennas: (a) a 10 cm. radius toroid adjacent to the borehole's wall, and (b) a 1 cm. radius toroid located at the borehole's center. The final log corresponding to the first difference of the magnetic field (normalized) is displayed in Fig. 7. In Fig. 8, we also display the final log corresponding to the first difference of the electric field (normalized), which has been computed according to the following postprocessing formula:

$$\mathbf{E}_z = \frac{1}{\sigma + j\omega \epsilon} (\nabla \times \mathbf{H})_z = \frac{1}{\sigma + j\omega \epsilon} \left[ \frac{1}{\rho} H_\phi + \frac{\partial H_\phi}{\partial \rho} \right]. \quad (31)$$

Results indicate a decay in the amplitude of the electromagnetic fields as the frequency increases. Nevertheless, the relative variations in the logging instrument response is almost frequency independent. In other words, if the scales were not present, we would not be able to distinguish between the field amplitude curves corresponding to different frequencies.

Results also show that the amplitude of the magnetic field decays as we decrease the radius of the transmitter and receiver toroids. However, the electric field amplitude does not decrease significantly. Finally, notice that the electric field response is slightly more sensitive to the rock formation conductivity for toroids adjacent to the borehole's wall, thereby suggesting the convenience of using this type of antennas for the assessment of electrical conductivity behind casing.

In Fig. 9 we display the (normalized) first difference of the electromagnetic fields as a function of the frequency, with the receiver antennas located at 0.4 m and 0.6 m, respectively. Notice the exponential decay of the fields, and the rapid variations in phase at high frequencies.

## VI. CONCLUSIONS

In this paper, we have simulated TCRT at DC and AC, as well as in the presence of damaged casing. High-accuracy simulations for these logging instruments have been obtained with a self-adaptive goal-oriented  $hp$ -FEM.

From these simulations, we conclude that Kaufmann's approximation formulas contain large errors (up to 25 % relative errors in the linear scale) if the rock formation resistivity is large. We also show that, in the presence of casing, the logging instrument response is highly sensitive to the thickness of the formation layers. Finally, we describe the possibility of using calibrated instruments when considering a damaged casing, and we study the inconvenience of placing small toroid

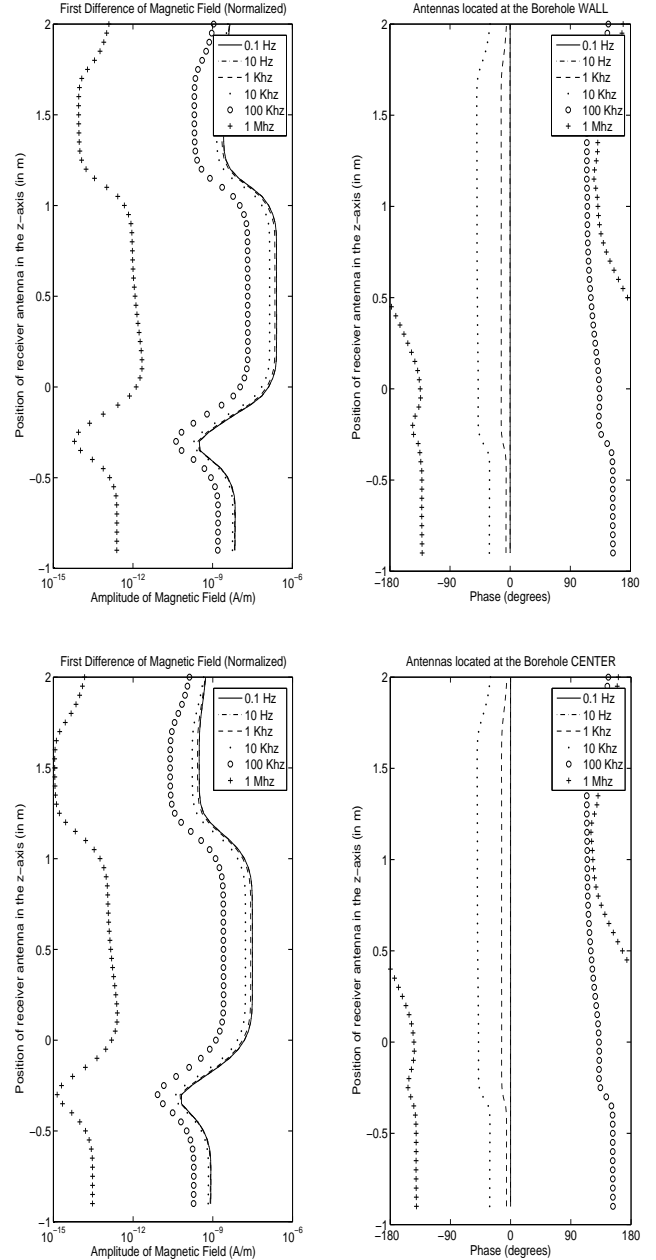


Fig. 7. TCRT problem. First difference of the magnetic field against position in the z-axis of the middle point between the two receiver antennas (in meters). We display amplitude (left panel) and phase (right panel) for antennas situated at the borehole wall (top) and at the center of the borehole (bottom).

antennas close to the axis of symmetry rather than on the borehole walls.

Results also indicate the possibility of using TCRT even for high frequencies, provided that accurate electronic devices could be manufactured to acquire the measurements.

## ACKNOWLEDGMENTS

We would like to thank Lev Tabarovsky and the Science Department of Baker-Atlas for their invaluable suggestions and advice.

## APPENDIX

### THE SELF-ADAPTIVE GOAL-ORIENTED $hp$ -FEM

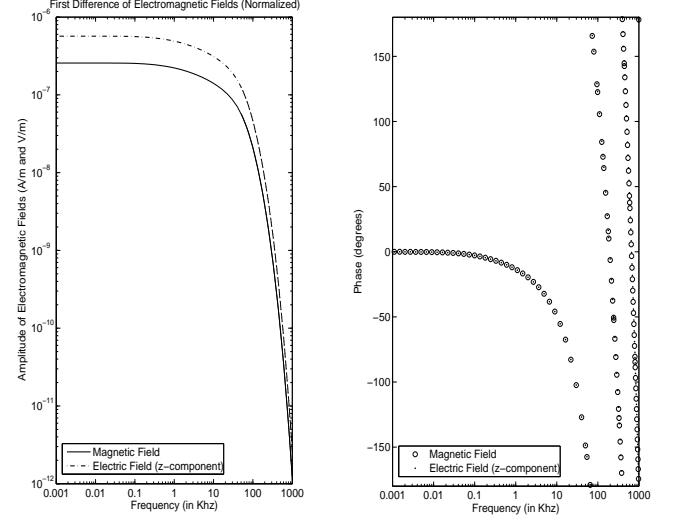
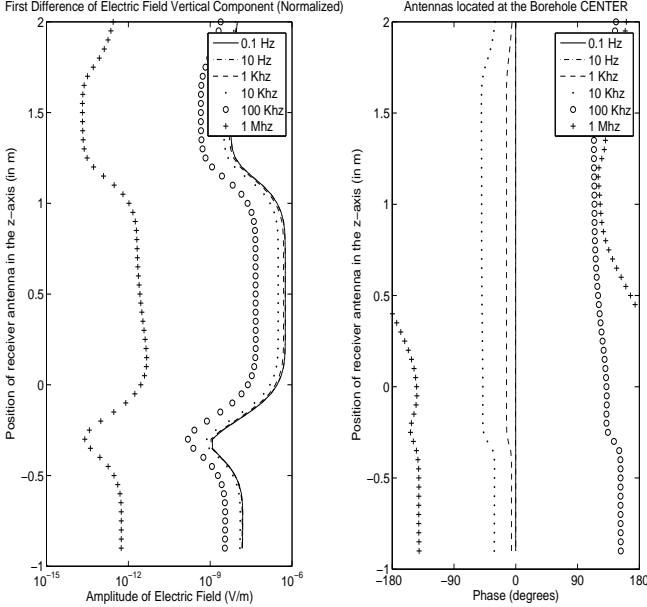
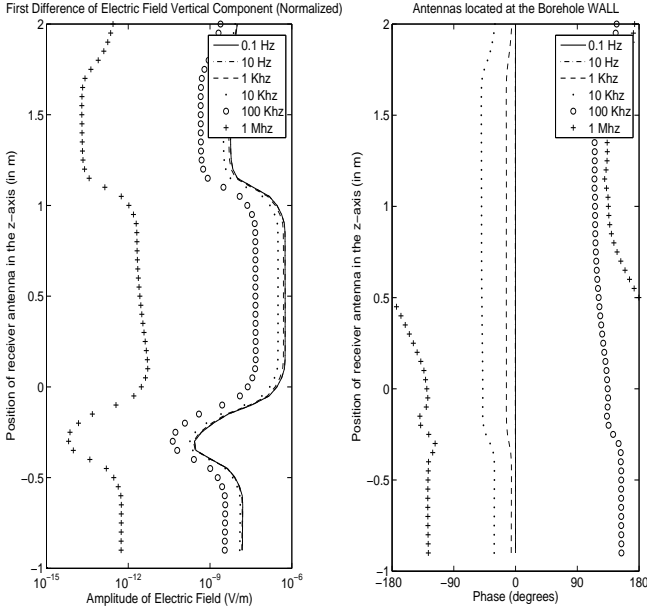


Fig. 9. TCRT problem. Frequency dependence of the first difference of the electromagnetic fields. We display amplitude (left panel) and phase (right panel) for antennas situated at the borehole wall at points  $z = 0.4$  m and  $z = 0.6$  m, respectively.

where  $e = u - u_{hp}$  denotes the error function. By defining the residual  $r_{hp} \in V'$  as  $r_{hp}(v) = f(v) - b(u_{hp}, v) = b(u - u_{hp}, v) = b(e, v)$ , we look for the solution of the *dual problem*:

$$\begin{cases} \text{Find } w \in V \\ b(v, w) = L(v) \quad \forall v \in V. \end{cases} \quad (34)$$

Using the Lax-Milgram theorem we conclude that problem (34) has a unique solution in  $V$ . The solution,  $w$ , is usually referred to as the *influence function*.

By discretizing (34) via, for example,  $V_{hp} \subset V$ , we obtain:

$$\begin{cases} \text{Find } w_{hp} \in V_{hp} \\ b(v_{hp}, w_{hp}) = L(v_{hp}) \quad \forall v_{hp} \in V_{hp}. \end{cases} \quad (35)$$

Due to the symmetry of the bilinear form  $b$  and the use of the same space  $V_{hp}$  for solving both (32) and (35), it is only necessary to factorize the system of linear equations once. Thus, the extra cost of solving (35) reduces to only one backward and forward substitution (if a direct solver is used).

By orthogonality of  $e$  with respect to  $V_{hp}$  (in the  $b$ -inner product), we have  $b(e, v_{hp}) = 0$  for all  $v_{hp} \in V_{hp}$ . Defining  $\epsilon = \epsilon(v_{hp}) = w - v_{hp}$ , we obtain :

$$E = L(e) = b(e, \epsilon). \quad (36)$$

Once the error  $E$  in the quantity of interest has been determined in terms of the bilinear form, we wish to obtain a sharp upper bound for  $|E|$  that utilizes only *local and computable* quantities. Then, a self-adaptive algorithm intended to minimize this bound will be defined.

First, using a similar procedure to the one described in [12], we approximate  $u$  and  $w$  with *fine grid* functions  $u_{\frac{h}{2}, p+1}$ ,  $w_{\frac{h}{2}, p+1}$ , which have been obtained by solving iteratively the corresponding linear system of equations associated with the FE subspace  $V_{\frac{h}{2}, p+1}$ . In the remainder of this paper,  $u$  and  $w$  will denote the fine grid solutions of the direct and dual problems ( $u = u_{\frac{h}{2}, p+1}$ , and  $w = w_{\frac{h}{2}, p+1}$ , respectively), and we will restrict ourselves to discrete FE spaces only.

Fig. 8. TCRT problem. First difference of the z-component of the electric field against position in the z-axis of the middle point between the two receiver antennas (in meters). We display amplitude (left panel) and phase (right panel) for antennas situated at the borehole wall (top) and at the center of the borehole (bottom).

In this appendix, we outline the main ideas of the self-adaptive goal-oriented  $hp$ -algorithm.

Given an  $hp$ -FE subspace  $V_{hp} \subset V$ , we discretize (29) as follows:

$$\begin{cases} \text{Find } u_{hp} \in u_D + V_{hp} \\ b(u_{hp}, v_{hp}) = f(v_{hp}) \quad \forall v_{hp} \in V_{hp}. \end{cases} \quad (32)$$

The objective of goal-oriented adaptivity is to construct an optimal  $hp$ -grid, in the sense that it minimizes the problem size needed to achieve a given tolerance error for a given *quantity of interest*  $L \in V'$ . By recalling the linearity of  $L$ , we have:

$$E = L(u) - L(u_{hp}) = L(u - u_{hp}) = L(e), \quad (33)$$

Next, we bound the error in the quantity of interest by a sum of element contributions. Let  $b_K$  be defined as  $b_K(u_K, v_K) = b(u_K, v_K)$  for all  $u_K, v_K \in V_K$ , where  $V_K \subset V$ . It then follows that:

$$|E| = |b(e, \epsilon)| \leq \sum_K |b_K(e, \epsilon)|, \quad (37)$$

where summation over  $K$  indicates summation over elements. The inner product and norm associated with the bilinear form  $b_K$  will be denoted as  $(\cdot, \cdot)_K$  and  $\|\cdot\|_K$ , respectively.

At this point, we introduce the *projection-based interpolation* operator  $\Pi_{hp} : V \rightarrow V_{hp}$  defined in [13], and used in [12], [14] for the construction of the fully automatic energy-norm based  $hp$ -adaptive algorithm. We define  $P_{hp} : V \rightarrow V_{hp}$  as the  $b$ -projection, and we denote  $u_{hp} = P_{hp}u$ . Then, taking the triangular inequality, (37) becomes:

$$|E| \leq \sum_K |b_K(u - \Pi_{hp}u, \epsilon) + b_K(\Pi_{hp}u - P_{hp}u, \epsilon)|. \quad (38)$$

Given an element  $K$ , it is expected that  $|b_K(\Pi_{hp}u - P_{hp}u, \epsilon)|$  will be negligible compared to  $|b_K(u - \Pi_{hp}u, \epsilon)|$ . Under this assumption, we conclude for the particular case  $\epsilon = w - \Pi_{hp}w$ :

$$|E| \leq \sum_K |b_K(u - \Pi_{hp}u, w - \Pi_{hp}w)|. \quad (39)$$

By applying the Cauchy-Schwartz inequality to the last equation, we obtain the next upper bound for  $|E|$ :

$$|E| \leq \|\tilde{e}\|_K \|\tilde{\epsilon}\|_K, \quad (40)$$

where  $\tilde{e} = u - \Pi_{hp}u$ , and  $\tilde{\epsilon} = w - \Pi_{hp}w$ .

Finally, we define the goal-oriented  $hp$  self-adaptive algorithm based on the main ideas of the fully automatic (energy-norm based)  $hp$ -adaptive algorithm presented in [12], [14]. We start by recalling the main objective of the self-adaptive (energy-norm based)  $hp$ -refinement strategy, which consists of solving the following maximization problem:

$$\left\{ \begin{array}{l} \text{Find an optimal } \tilde{hp}\text{-grid in the following sense:} \\ \tilde{hp} = \arg \max_{\tilde{hp}} \sum_K \frac{|\tilde{\epsilon}_K|_{1,K}^2 - |\hat{\epsilon}_K|_{1,K}^2}{\Delta N}, \end{array} \right. \quad (41)$$

where

- $\tilde{e}_K = u - \Pi_{hp}^K u$  and  $\hat{e}_K = u - \Pi_{\tilde{hp}}^K u$ .
- $u = u_{\frac{h}{2}, p+1}$  is the *fine grid* solution,
- $\Delta N > 0$  is the increment in the number of unknowns from grid  $hp$  to grid  $\tilde{hp}$ , and
- $|\cdot|_{1,K}$  is the  $H^1$ -seminorm for element  $K$ .

Similarly, for goal-oriented  $hp$ -adaptivity, we propose the following algorithms based on estimate (40):

$$\left\{ \begin{array}{l} \text{Find an optimal } \tilde{hp}\text{-grid in the following sense:} \\ \tilde{hp} = \arg \max_{\tilde{hp}} \sum_K \frac{|\tilde{\epsilon}_K|_{1,K} \cdot |\tilde{\epsilon}_K|_{1,K}}{\Delta N} - \frac{|\hat{\epsilon}_K|_{1,K} \cdot |\hat{\epsilon}_K|_{1,K}}{\Delta N}, \end{array} \right. \quad (42)$$

where:

- $\tilde{e}_K = u - \Pi_{hp}^K u$ ,  $\hat{e}_K = u - \Pi_{\tilde{hp}}^K u$ ,  $\tilde{\epsilon}_K = w - \Pi_{hp}^K w$ , and  $\hat{\epsilon}_K = w - \Pi_{\tilde{hp}}^K w$ .
- $u = u_{\frac{h}{2}, p+1}$  and  $w = w_{\frac{h}{2}, p+1}$  are the *fine grid* solutions corresponding to the direct and dual problems,
- $\Delta N > 0$  is the increment in the number of unknowns from grid  $hp$  to grid  $\tilde{hp}$ , and
- $|\cdot|_{1,K}$  is the  $H^1$ -seminorm for element  $K$ .

Implementation of the goal-oriented  $hp$ -adaptive algorithm is based on the optimization procedure used for energy-norm  $hp$ -adaptivity [14].

Fig. 10 shows an example of an automatically generated  $hp$ -grid for a TCRT problem. This grid delivers a relative error on the first difference of the magnetic field (measured on the receiving antennas) below 3%. In this case, the adaptive algorithm has selected higher order elements for approximating the exact solution in the rock formation, but neither in the borehole nor in the casing, thereby suggesting that the solution in the borehole and in the casing exhibits a quasi-linear behavior.

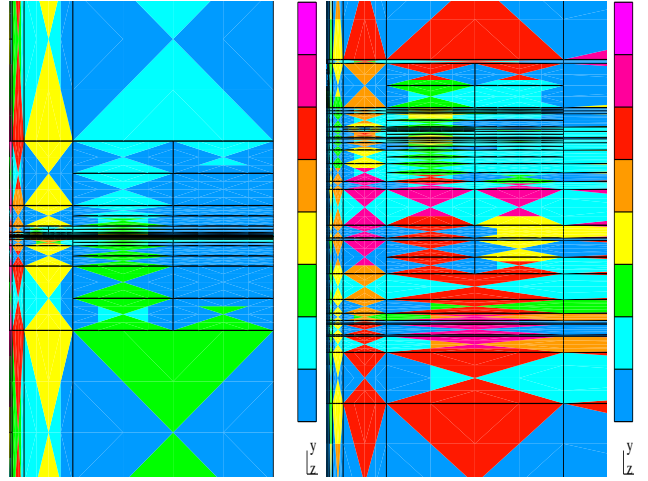


Fig. 10. TCRT problem. Final  $hp$ -grid delivering a relative error of the first difference of the magnetic field measured on the receiving antennas below 3%. Different colors indicate different polynomial degrees of approximation, ranging from 1 (dark blue) to 8 (pink). The dimensions of the displayed grid are 500m (horizontal) x 1000m (vertical) on the left panel and 2m (horizontal) x 4m (vertical) on the right panel.

## REFERENCES

- [1] A. A. Kaufman, "The electrical field in a borehole with casing." *Geophysics*, vol. 55, no. 1, pp. 29–38, 1990.
- [2] W. Vail, S. Momii, R. Woodhouse, M. Alberty, R. Peveraro, and J. Klein, "Formation Resistivity Measurements Through Metal Casing." *SPWLA 34th Annual Logging Symposium*, vol. F, 1993.
- [3] C. J. Schenkel and H. F. Morrison, "Electrical resistivity measurement through metal casing." *Geophysics*, vol. 59, no. 7, pp. 1072–1082, 1994.
- [4] X. Wu and T. M. Habashy, "Influence of Steel Casings on Electromagnetic Signals." *Geophysics*, vol. 59, no. 3, pp. 378–390, 1994.
- [5] I. Babuska and A. Miller, "The post-processing approach in the finite element method. I. Calculation of displacements, stresses and other higher derivatives of the displacements." *Int. J. Numer. Methods Eng.*, vol. 20, pp. 1085–1109, 1984.
- [6] D. Pardo, L. Demkowicz, and C. Torres-Verdin, "A Goal Oriented  $hp$ -Adaptive Finite Element Method with Electromagnetic Applications. Part I: Electrostatics." *ICES Report 04-57. Submitted to Int. J. Numer. Methods Eng.*, vol. 0, p. 0, 2005.
- [7] W. Cecot, W. Rachowicz, and L. Demkowicz, "An  $hp$ -adaptive finite element method for electromagnetics. III: A three-dimensional infinite element for Maxwell's equations." *Int. J. Numer. Methods Eng.*, vol. 57, no. 7, pp. 899–921, 2003.

- [8] I. Babuska and B. Q. Guo, "Regularity of the solution of elliptic problems with piecewise analytic data. I. Boundary value problems for linear elliptic equation of second order," *SIAM J. Math. Anal.*, vol. 19, no. 1, pp. 172–203, 1988.
- [9] I. Babuska and B. Guo, "Approximation properties of the  $h$ - $p$  version of the finite element method." *Comput. Methods Appl. Mech. Eng.*, vol. 133, no. 3-4, pp. 319–346, 1996.
- [10] C. Schwab,  *$p$ - and  $hp$ -finite element methods*, ser. Numerical Mathematics and Scientific Computation. New York: The Clarendon Press Oxford University Press, 1998, theory and applications in solid and fluid mechanics.
- [11] J. R. Lovell, "Finite Element Methods in Resistivity Logging," Ph.D. dissertation, Delft University of Technology, 1993.
- [12] L. Demkowicz, W. Rachowicz, and P. Devloo, "A fully automatic  $hp$ -adaptivity." *J. Sci. Comput.*, vol. 17, no. 1-4, pp. 117–142, 2002.
- [13] L. Demkowicz and A. Buffa, " $H^1$ ,  $H(\text{curl})$ , and  $H(\text{div})$  conforming projection-based interpolation in three dimensions: quasi optimal  $p$ -interpolation estimates." *Comput. Methods Appl. Mech. Eng.*, vol. 194, pp. 267–296, 2005.
- [14] W. Rachowicz, D. Pardo, and L. Demkowicz, "Fully automatic  $hp$ -adaptivity in three dimensions." ICES Report, Tech. Rep. 04-22, 2004.



**David Pardo** received his B.S. (2000) degree in Mathematics from the University of The Basque Country, Spain, and M.S. (2002) and Ph.D.(2004) in Computational and Applied Mathematics from The University of Texas at Austin. He is currently working as a Postdoctoral Fellow at the Institute for Computational Engineering and Sciences at The University of Texas at Austin. His research interests include Computational Electromagnetics, Petroleum Engineering applications, Adaptive Finite Element Methods, and Multigrid Solvers.



**Carlos Torres-Verdín** is an Associate Professor in the Department of Petroleum and Geosystems Engineering at The University of Texas at Austin. He holds a B.S. in Geophysical Engineering from the National Polytechnic Institute of México, a M.Sc. in Electrical Engineering from The University of Texas at Austin, and a Ph.D. in Engineering Geoscience from the University of California, Berkeley. He has published on the topics of electromagnetic geophysics, numerical simulation, inverse theory, reservoir characterization, and 3-D reflection seismology.

He worked 2 years for the oil company YPF, in Buenos Aires, Argentina, and 5.5 years for Schlumberger-Doll Research in Ridgefield, Connecticut.



**Leszek F. Demkowicz** is a Professor in the Department of Aerospace Engineering and Engineering Mechanics at The University of Texas at Austin. Since 1993, he has served as an Assistant Director of the Institute for Computational Engineering and Sciences (ICES) at The University of Texas at Austin. He graduated cum laudae from Cracow University of Technology in 1976 with M.S. in Engineering Mechanics and from Jagiellonian University in Cracow in 1978 with M.S. in Theoretical Mathematics. He received a Ph.D. in Engineering in 1982 from The

Cracow University of Technology, Poland. Dr. Demkowicz edited two books, has authored and co-authored two books, has published over 100 papers, and over 35 technical reports (unpublished elsewhere). He serves on the editorial board of four international journals. His area of expertise includes Functional Analysis, Numerical Analysis,  $h$ ,  $p$ , and  $hp$  Adaptive Finite Element Methods with applications to solid and fluid mechanics, elasticity, acoustics and electromagnetic wave propagation.